








# Autoencoding Galaxy Spectra. II. Redshift Invariance and Outlier Detection

Yan Liang<sup>1</sup> , Peter Melchior<sup>1,2</sup> , Sicong Lu<sup>3</sup> , Andy Goulding<sup>1</sup> , and Charlotte Ward<sup>1</sup> <sup>1</sup>Department of Astrophysical Sciences, Princeton University, Princeton, NJ 08544, USA; [yanliang@princeton.edu](mailto:yanliang@princeton.edu)<sup>2</sup>Center for Statistics & Machine Learning, Princeton University, Princeton, NJ 08544, USA<sup>3</sup>Department of Physics and Astronomy, University of Pennsylvania, Philadelphia, PA 19104, USA

Received 2023 February 5; revised 2023 May 12; accepted 2023 May 16; published 2023 July 27

## Abstract

We present an unsupervised outlier detection method for galaxy spectra based on the spectrum autoencoder architecture SPENDER, which reliably captures spectral features and provides highly realistic reconstructions for SDSS galaxy spectra. We interpret the sample density in the autoencoder latent space as a probability distribution, and identify outliers as low-probability objects with a normalizing flow. However, we found that the latent-space position is not, as expected from the architecture, redshift invariant, which introduces stochasticity into the latent space and the outlier detection method. We solve this problem by adding two novel loss terms during training, which explicitly link latent-space distances to data-space distances, preserving locality in the autoencoding process. Minimizing the additional losses leads to a redshift-invariant, nondegenerate latent-space distribution with clear separations between common and anomalous data. We inspect the spectra with the lowest probability and find them to include blends with foreground stars, extremely reddened galaxies, galaxy pairs and triples, and stars that are misclassified as galaxies. We release the newly trained SPENDER model and the latent-space probability for the entire SDSS-I galaxy sample to aid further investigations.

*Unified Astronomy Thesaurus concepts:* [Galaxies \(573\)](#); [Spectroscopy \(1558\)](#); [Astrostatistics \(1882\)](#)

## 1. Introduction

Spectroscopy is a critical tool to probe the physical mechanisms that drive the formation and evolution of galaxies. Despite the vast amount of available galaxy spectra provided by large spectroscopic surveys, extracting physical knowledge from them is still a difficult task. Ideally, one would infer galaxy properties by directly fitting the observed spectrum to a theoretical model, but analytical models are not yet sophisticated enough to reproduce typical individual high S/N galaxy spectra, especially the strong emission lines (Tojeiro et al. 2007, 2011). The physical processes contributing to the observed spectral features may be still poorly understood, thus using oversimplified models could lead to a biased interpretation of the data.

Alternatively, one may construct a fully data-driven model via unsupervised learning. The main challenge in this approach is to properly disentangle the intrinsic physical spectra from redshift (causing a stretching of the spectra), noise level, and artifacts such as telluric contamination. Linear models, i.e., a combination of empirical or theoretical templates (Polletta et al. 2007; Brown et al. 2014), are commonly used for redshift estimation and spectral classification (Bolton et al. 2012; Pace et al. 2019; Ross et al. 2020). The reconstruction power of linear models is limited by template quality, and often requires many components to achieve a good fit. On the other hand, machine-learning (ML) techniques, such as unsupervised random forest (Baron & Poznanski 2017) and self-organizing maps (Hoyle et al. 2015), are used for outlier detection without producing a reconstruction.

Autoencoders (AE) can yield models with good fidelity and small latent dimensionality (Portillo et al. 2020). But for

conventional AEs (and other unsupervised ML methods), all galaxy spectra needed to be deredshifted and resampled to a common rest frame, restricting either redshift or wavelength ranges that can be probed. In an earlier work, we showed that by explicitly adding a redshift transformation to the decoder path, one can utilize the entire spectrum for galaxies at all redshifts (Melchior et al. 2023). This new architecture called SPENDER effectively compresses SDSS spectra into a low-dimensional latent space, where positions should be invariant under changes of the redshift because they are meant to encode galaxy “types,” with the redshift transformation only affecting the last stage of the generator (see Figure 1). In Section 3, we demonstrate this expectation to be naïve. The generator network’s flexibility enables it to map different latent-space positions to strikingly similar rest-frame spectra, allowing the autoencoder to adopt multiple solutions for representing the same galaxy spectrum, with no penalty in case it chooses a different one at a different redshift. This observation demonstrates the importance of constraining the model capacity to prevent overfitting and improve the model’s generalization capabilities.

We then propose a strategy to lift this degeneracy with training on augmented spectra, whose redshifts we have altered, and a similarity metric that relates latent-space distances to distances between reconstructed spectra. At very minor reduction in fidelity, minimizing the additional losses makes the latent space robustly invariant to changes in redshift, observation windows, and noise levels. The encoded parameters become directly interpretable—the spectra of physically similar galaxies cluster in latent space, and positions in the same neighborhood reconstruct similar-looking spectra.

The interpretability of the latent space enables the discovery of trends and clusters in high-dimensional data, and the characterization of individual objects in a meaningful context (Section 4). It further allows for the identification of rare or extreme objects in the sample that could potentially reveal new



Original content from this work may be used under the terms of the [Creative Commons Attribution 4.0 licence](#). Any further distribution of this work must maintain attribution to the author(s) and the title of the work, journal citation and DOI.

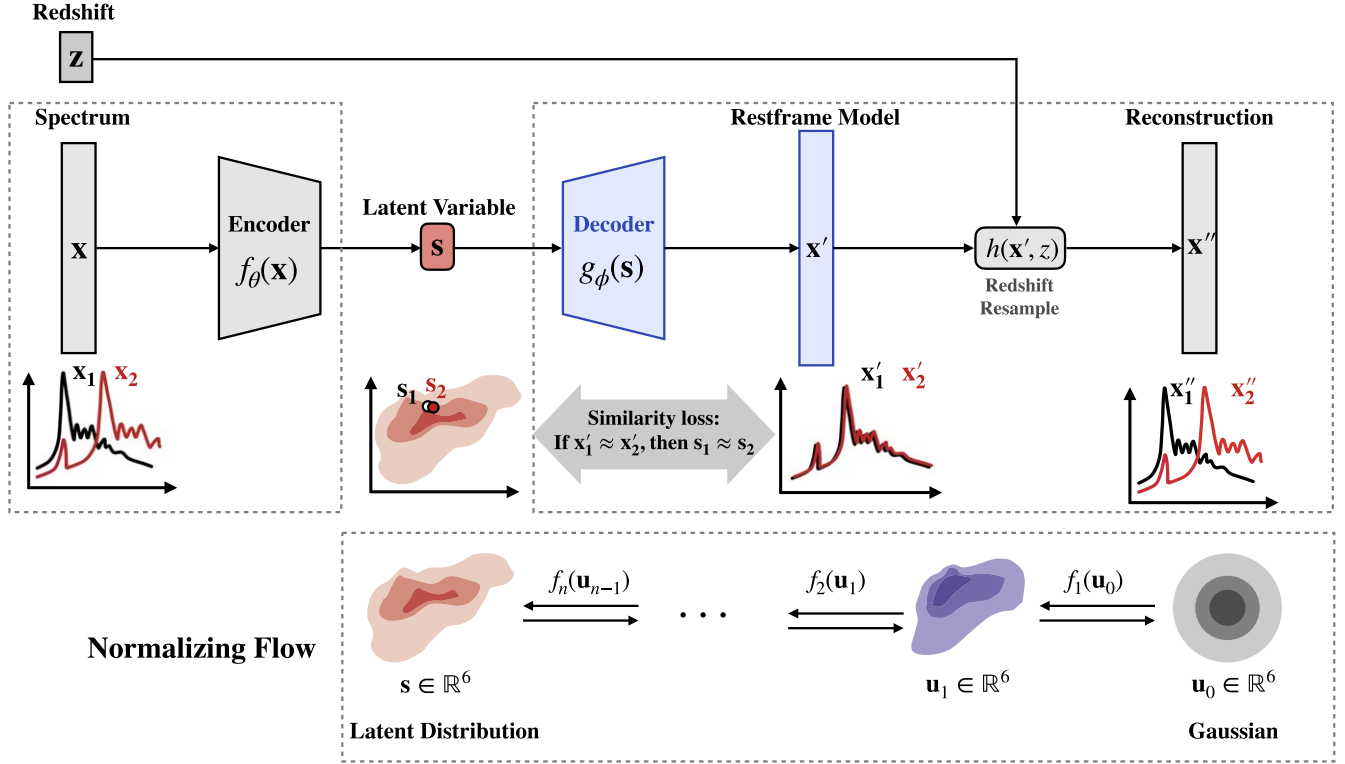


**Figure 1.** The autoencoder SPENDER generates a rest frame and observed spectrum reconstruction. It is trained with a conventional fidelity loss, which compares separately input spectra  $(x_1, x_2)$  to their redshifted and resampled reconstructions  $(x'_1, x'_2)$ . In this work, we added a novel similarity loss, which links the distance in latent space  $|s_1 - s_2|$  between two spectra to their distance in rest frame  $|x'_1 - x'_2|$ . Spectra of two physically similar galaxies observed at different redshifts  $(z_1, z_2)$ , for which the underlying rest-frame models are very similar, will thus yield similar latent vectors. To further improve the encoding stability, we minimize an additional consistency loss defined as the latent distances between the input spectra and its artificially redshifted augment  $|s_i - s_{i,\text{aug}}|$ . After training the autoencoder, we train a normalizing flow to map the complicated latent distribution of the entire SDSS galaxy sample to a Gaussian base distribution through a series of invertible transformations, which allows efficient computation of the probability of any given sample.

physics, which we will investigate in Section 5. We also point out, but do not explore in this work, that our new latent space representation supports the creation of realistic mock spectra through sampling from the latent space. We conclude in Section 6 with a discussion of the potential uses of this method and the prospects of extending it to future surveys.

## 2. Data

We select  $\sim 500,000$  galaxy spectra spanning redshift  $z \in [0, 0.5]$  from Sloan Digital Sky Surveys Data Release 16 (Ahumada et al. 2020). Our sample includes all optical spectra that are classified as galaxies and have redshift error  $z_{\text{err}} < 10^{-4}$ . Approximately 70% of the samples are used for training, 15% for validation, and 15% is held for testing. All spectra are zero padded to a homogeneous wavelength  $\lambda_{\text{obs}} = 3784 \dots 9332 \text{ \AA}$ . We use inverse-variance weights and masks provided by SDSS Data Release 16 as flux uncertainties. Additionally, we mask out telluric contamination by assigning zero weights to within  $5 \text{ \AA}$  of the top  $\sim 100$  telluric lines, amounting to 12% of the data vectors. All spectra are normalized by the median flux over rest-frame wavelengths  $\lambda_{\text{rest}} = 5300 \dots 5850 \text{ \AA}$ . The rest-frame normalization is chosen to be relatively quiet and accessible at all redshifts to avoid redshift-dependent amplitudes.

## 3. Method

Our model architecture is taken from Melchior et al. (2023; see Figure 1 for an overview and the aforementioned paper for details).

Let  $x \in \mathbb{R}^M$  denote an input spectrum with  $M = 3921$  elements. It gets encoded, by a modified version of the CNN encoder from Serrà et al. (2018), into a low-dimensional latent representation,  $s \in \mathbb{R}^S$ . While the architecture can have arbitrary latent dimensions, we choose  $S = 6$ , which provides a good trade-off between the reconstruction quality and model complexity, as suggested by Melchior et al. (2023). A standard MLP with (256, 512, 1024) nodes and a leaky ReLU activation generates a rest-frame spectrum  $x'$ , whose 7000 spectral elements are chosen to create a mildly superresolved representation with an extended wavelength coverage ( $\lambda_{\text{rest}} = 2359 \dots 9332 \text{ \AA}$ ). The reconstructed spectrum  $x''$  is then redshifted and linearly interpolated from  $x'$  to the same wavelengths as  $x$ .

This architecture allows for a redshift-invariant latent encoding because the redshift transformation is explicitly performed in the generator. One might therefore expect that the network will use the same latent variables to represent the same rest-frame spectrum at all redshifts as that would simplify the decoding process. However, we find that the encoder network does not typically yield the same latent in this case. We arrive at this unintuitive finding by encoding ‘‘augmented’’ galaxy spectra, for which we have artificially altered the redshifts. The top panel of Figure 2 shows the distribution of Euclidean distances in latent space  $\Delta s_{\text{aug}}$  between the original and the augmented spectrum (in red), which has a comparable spread to the distance distribution of randomly selected original spectra (in blue). We interpret this result as the high flexibility of the architecture allowing the decoder to reconstruct indistinguishable models from different encoded locations. To achieve the best reconstructions across a range of spectral types and redshifts, the

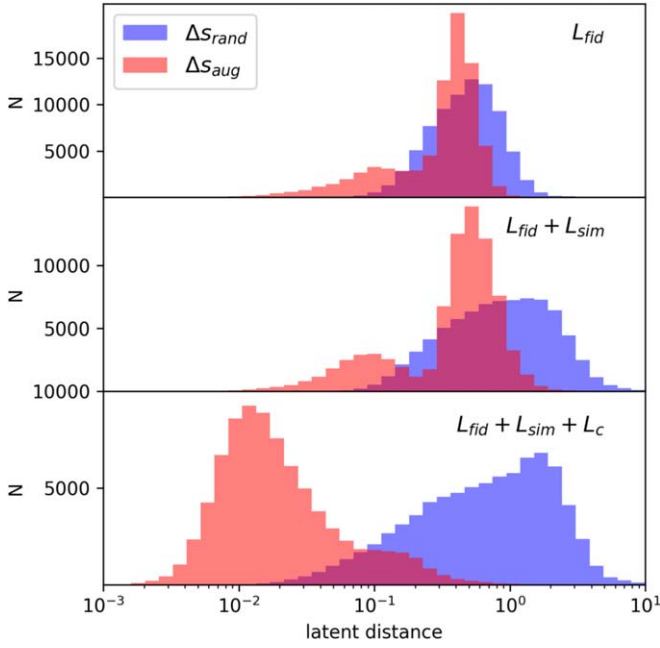


**Figure 2.** Euclidean distance distribution in latent space for randomly selected galaxy pairs ( $\Delta s_{rand}$ , blue) and original-augment pairs ( $\Delta s_{aug}$ ). Augmented spectra stem from the original spectra by artificially altering the redshifts. If the encoder is redshift invariant,  $\Delta s_{aug} = 0$ . The three panels refer to the result of training with different terms in the loss function Equation (2). Optimizing the full loss function (bottom) significantly reduces  $\Delta s_{aug}$ , while increasing  $\Delta s_{rand}$ , i.e., increasing the separation of different spectral types in latent space.

autoencoder employs its full capacity, including redshift-dependent encoding, to represent galaxy spectra. Without additional constraints, the model may “overfit” the data by generating distinct latents for intrinsically similar galaxies at different redshifts.

### 3.1. Loss Function

Our basic training in Melchior et al. (2023) used a conventional fidelity loss, which quantifies the reconstruction quality, assuming normally distributed noise. It measures the mean log-likelihood of the reconstruction of spectral elements averaged over batches of  $N$  spectra with spectral size  $M$ :

$$L_{fid} = \frac{1}{2NM} \sum_i^N \mathbf{w}_i \odot (\mathbf{x}_i - \mathbf{x}_i'')^2, \quad (1)$$

where  $\mathbf{x}_i$  is the  $i$ th input spectrum,  $\mathbf{w}_i$  its inverse variance, and  $\odot$  the element-wise multiplication.

A stronger constraint is required to generate robustly redshift-invariant encoding. Our extended loss function

$$L_{total} = L_{fid} + L_{sim} + L_c \quad (2)$$

operates on all four of the stages shown in Figure 1. We define a similarity loss  $L_{sim}$  that, unlike the fidelity loss, operates on the two intermediate stages. Let  $\mathbf{s} = f_\theta(\mathbf{x})$  be the encoded latent vector and  $\mathbf{x}' = g_\phi(\mathbf{s})$  be the rest-frame model, where  $f_\theta, g_\phi$  are parameterized encoder and decoder functions. Ideally, if two rest-frame models,  $\mathbf{x}_i'$  and  $\mathbf{x}_j'$  are similar, their latent positions  $\mathbf{s}_i$  and  $\mathbf{s}_j$  should be similar as well; otherwise, the mapping from latent space to spectrum space becomes difficult to interpret. On the other hand, distinctively different models should have well-separated latent positions. The desired relation can be

satisfied naturally if the latent distance is proportional to a spectral distance:  $|\mathbf{s}_i - \mathbf{s}_j|^2 \propto |\mathbf{x}_i' - \mathbf{x}_j'|^2$ , which motivates us to set up a loss term as follows:

$$L_{sim}(\mathcal{S}, k_0, k_1) = \frac{1}{N^2} \sum_{i,j} \text{sigmoid}(k_1 S_{i,j} - k_0) + \frac{1}{N^2} \sum_{i,j} \text{sigmoid}(-k_1 S_{i,j} - k_0), \quad (3)$$

where

$$S_{i,j} = \frac{1}{S} |\mathbf{s}_i - \mathbf{s}_j|^2 - \frac{1}{M} |\mathbf{w}' \odot (\mathbf{x}_i' - \mathbf{x}_j')|^2, \quad (4)$$

$\mathbf{w}'$  is the inverse-variance weight defined at rest-frame wavelengths, and  $k_0, k_1$  are adjustable hyper-parameters that control the steepness of the slope.  $L_{sim}$  encourages pair-wise latent space distances to be proportional to the spectra (dis)similarity defined in Equation (4). For a batch of  $N$  spectra, we compare each rest-frame spectrum  $\mathbf{x}_i'$  to every other rest-frame spectrum  $\mathbf{x}_j'$ , and calculate the pair-wise distances as a  $N \times N$  matrix. If the rest-frame models  $\mathbf{x}_i'$  and  $\mathbf{x}_j'$  are similar but have a large latent distance, the first sigmoid term brings them closer in latent space. Conversely, if the rest-frame models are dissimilar but have a small latent distance, the second sigmoid term pushes them apart. Optimizing  $L_{sim}$  drives  $S_{i,j}$  toward zero. In each iteration of the optimization process, the batches are randomly reassembled so that pair-wise distances can be computed across the entire data set.

The double sigmoid function in Equation (3) serves two purposes. It limits the effect of the similarity loss by setting  $L_{sim} \leq 1$ , such that it is only important when the fidelity loss is also comparably low,  $L_{fid} \lesssim 1$ . It provides relatively smooth gradients (compared to e.g.,  $S_{i,j}^2$ ), improving the trainability of the model. It is crucial to measure the similarity between rest-frame pairs rather than input pairs, because the former provides a stable measure independent of redshift and observational window. In addition, rest-frame models usually contain less noise than the original data (see Figure 3, bottom-left panel).

Inspired by Sinha & Dieng (2021), we add the consistency loss as a more guided form of the similarity loss:

$$L_c = \frac{1}{N} \sum_i^N \text{sigmoid} \left[ \frac{1}{\sigma_s^2 S} |\mathbf{s}_i - \mathbf{s}_{aug,i}|^2 \right] - 0.5 \quad (5)$$

where  $\mathbf{s}_i$  and  $\mathbf{s}_{aug,i}$  are the latent positions of the original and its corresponding augment spectrum, that has been redshifted by a random  $z_{new}$  from a uniform distribution between  $[0, 0.5]$ . In practice, we set  $\sigma_s = 0.1$  which provides a good trade-off between the consistency and the overall scale of the latent distribution. Minimizing  $L_c$  reduces the latent distances between galaxy spectra and their augments, improving the encoding stability against redshift variation. The consistency loss reinforces that physically similar spectra pairs are pulled together in latent space, while dissimilar pairs are moved apart by the (dis)similarity loss term (Equation (4)). This combination of losses should make the latent space also more expressive by encouraging of clustering of similar and separation of dissimilar spectra, which we will exploit in Section 5.

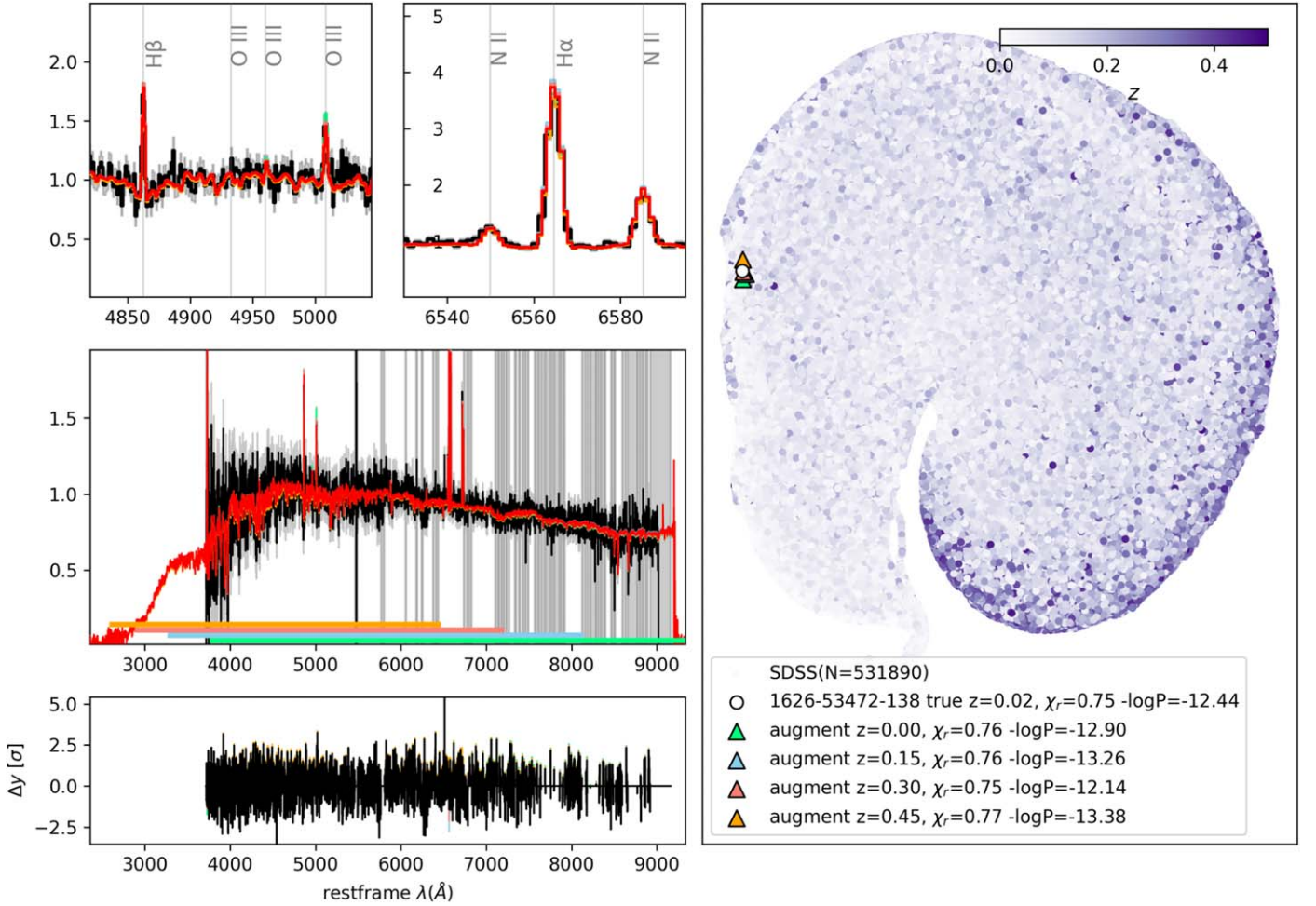


**Figure 3.** Left: observed spectrum (black) of a galaxy from the test sample at  $z = 0.02$ , its reconstruction (red), and reconstructions of augmented spectra with artificially altered redshifts (color-coded). Zoomed-in versions are shown on the top. The colored bar in the middle-left shows the observed wavelength range of the augments. Right: UMAP-embedded latent space distribution of the entire SDSS galaxy sample. The white circle marks the example spectrum, and the triangles mark its augments.

**Table 1**  
Model Performance Comparison Using Different Training Strategies

Training objective	$L_{\text{fid}}$ (train)	$L_{\text{fid}}$ (valid)	$L_{\text{fid}}$ (test)	$L_{\text{sim}}$	$L_c$	$\langle \Delta s_{\text{aug}} \rangle$	$\langle \Delta s_{\text{rand}} \rangle$	$\langle \Delta s_{\text{aug}} \rangle / \langle \Delta s_{\text{rand}} \rangle$
$L_{\text{fid}}$	0.385	0.386	0.387	...	...	0.353	0.540	65.4%
$L_{\text{fid}} + L_{\text{sim}}$	0.387	0.388	0.388	0.177	...	0.483	1.232	39.2%
$L_{\text{fid}} + L_{\text{sim}} + L_c$	0.388	0.390	0.389	0.177	0.020	0.043	1.103	3.9%

**Note.** The fidelity loss,  $L_{\text{fid}}$ , is presented for the training, validation, and test sets for each of the three models. All other terms are evaluated on the test set.  $\langle \Delta s_{\text{aug}} \rangle$  denotes the average Euclidean distance between encoded data-augment pairs,  $\langle \Delta s_{\text{rand}} \rangle$  for randomly chosen data pairs. See Figure 2 for a visualization of the same data.  $L_{\text{sim}}$  is evaluated assuming  $k_0 = 2.5$ ,  $k_1 = 5.0$ . Note that when the latent distance and spectral distance are perfectly aligned, the minimum similarity loss  $L_{\text{sim}}$  is 0.151.

### 3.2. Training

To evaluate the impact of different loss terms, we trained three models using different strategies: In the first training, we optimize the model with  $L_{\text{fid}}$  alone to serve as the baseline. In the second model, we optimize  $L_{\text{fid}} + L_{\text{sim}}$  simultaneously, with an “inverse-annealing” cycle to gradually increase the slope  $k_1$ , while  $k_0$  is held constant. For the third model, we add the consistency regularization and optimize the full loss defined in Equation (2).

We train each model on an NVIDIA A100 GPU using the same training and validation data set for 1000 epochs and observe convergence. The results are summarized in Table 1 and Figure 2.

Our observations indicate no strong evidence of overfitting across the models, as seen through the consistency between training and validation/test fidelity. Additionally, incorporating the extra loss terms appears to yield a minor improvement in the agreement between training and testing fidelity. With the fidelity loss closely matched in all three runs, the best performance in terms of redshift invariance is achieved with all three losses combined. In particular, including the similarity loss  $L_{\text{sim}}$  encourages dissimilar spectra pairs to move apart (see Figure 2, middle panel), increasing the average latent distance between random spectra pairs by a factor of 2. Optimizing  $L_c$  along with  $L_{\text{fid}} + L_{\text{sim}}$  reduces the average latent distance of augmented redshifted spectra by a factor of  $\sim 10$ .

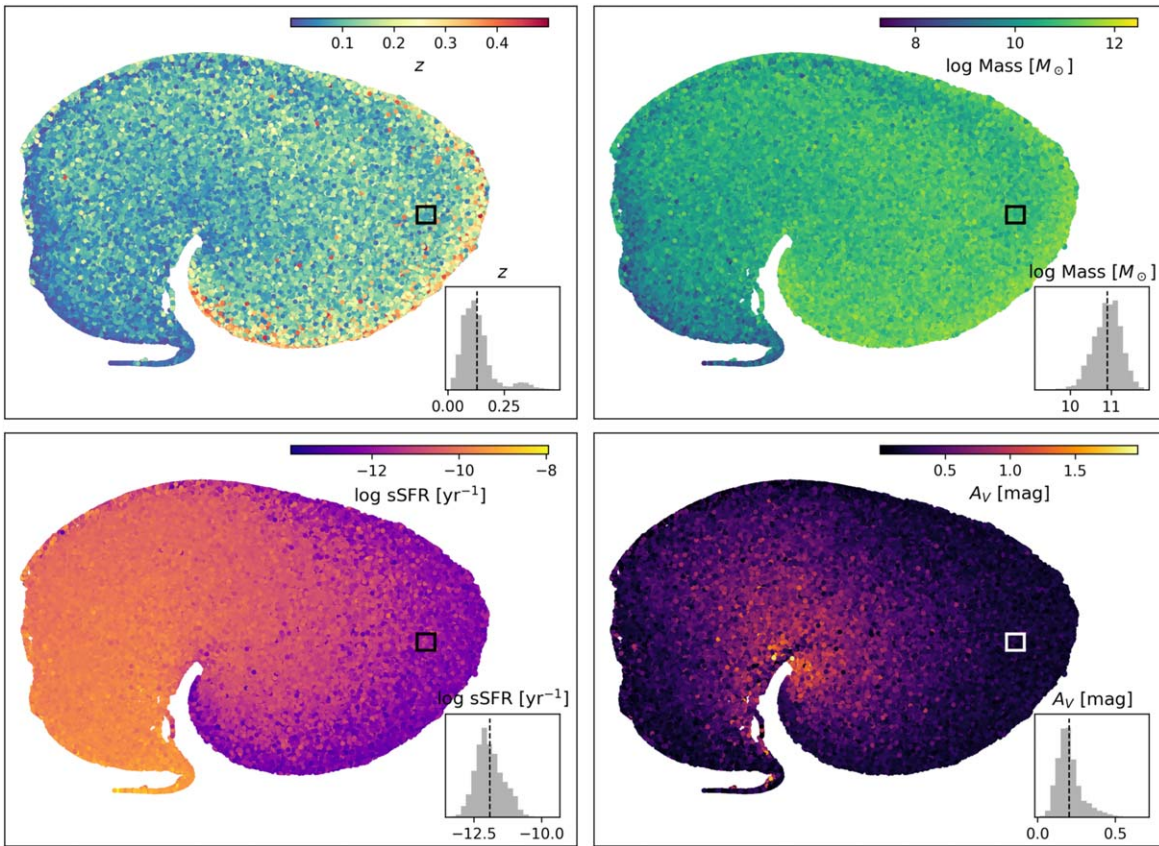


**Figure 4.** UMAP embedding of the latent variables for all 531,890 SDSS galaxy spectra, color-coded by redshifts (top left), stellar masses (top right), specific star-formation rates (lower left), and dust attenuation in rest-frame  $V$  band (lower right). The lower right histograms show the distribution of physical properties of  $\sim 2000$  samples located inside a small box (marked black/white) in the UMAP space.

(Figure 2, bottom panel). As a result, in the latent space of the best-fit model, the true and augmented spectra are 25 times closer to each other than the average pair-wise distance, while for the fidelity-alone model, the original and augmented spectra are only 1.5 times closer than the average. This order-of-magnitude improvement has been achieved with a very minor decrease in fidelity, which suggests that the autoencoder indeed has sufficient flexibility to accommodate the additional demands to the latent space without sacrificing reconstruction quality.

We suggest that the consistency loss should not be used without the similarity loss because it merely seeks to compress the volume occupied by the latent distribution and collapse it to a point at the origin. Instead, it is best added once a model trained with fidelity and similarity losses is available.

With the best model, we achieve a desirable redshift-invariant behavior. Figure 3 shows the reconstructed rest-frame model and encoded latent position for an example galaxy. The latent positions of the original and redshift-augmented spectra are stably grouped together (colored markers in the right panel), even for the  $z = 0.45$  augment (colored in orange) where the dominant  $H\alpha$  emission line is outside of the observable wavelength range, i.e., unavailable to the encoder. The reconstruction quality is evidently robust to such missing features.

#### 4. Latent-space Structure

Following the approach we took in Melchior et al. (2023), we inspect the latent space distribution by further projecting the latent variables of the entire galaxy spectra sample into a two-dimensional UMAP embedding (McInnes et al. 2018). As

shown in Figure 4, the UMAP embedding of the data set is continuous and connected. To test our assumption that the latent space encodes the physical properties of the galaxy without our supervision, we plot the stellar masses, star-formation rates, and dust attenuation estimates from the GALEX-SDSS-WISE LEGACY CATALOG (Salim et al. 2016, 2018), which covers  $\sim 80\%$  of the SDSS galaxy spectra.

As shown in Figure 4, the two-dimensional embedding of the latent space strongly correlates with each of the physical properties: the specific star-formation rate is predominantly following a continuous trend in the counter-clockwise direction, from the most quiescent galaxies to starburst galaxies (bottom-left panel). The stellar mass of galaxies correlates with the clockwise direction (top-right panel). The galaxies with the strongest dust attenuation seem to cluster around a “locus” where the star-forming and quiescent galaxies are squeezed together, and the attenuation weakens inside out in the radial direction (bottom-right panel).

One might notice that the stellar mass appears to correlate with redshift (top-left panel). As we have argued in Melchior et al. (2023), this is an artifact of a magnitude-limited sample. At high redshift, only the most massive galaxies are observed, while low-mass galaxies can be observed only at low redshifts.

By inspecting the latent space structures, we conclude that our latent space is well behaved and physically informative. One can, for instance, assign an estimate of the physical properties of an SDSS-I spectrum according to its neighbors in latent space. Similar approaches have been reported with direct embeddings, but have so far been restricted to, e.g., lower-dimensional spaces of broad-band SEDs (Hemmati et al. 2019)

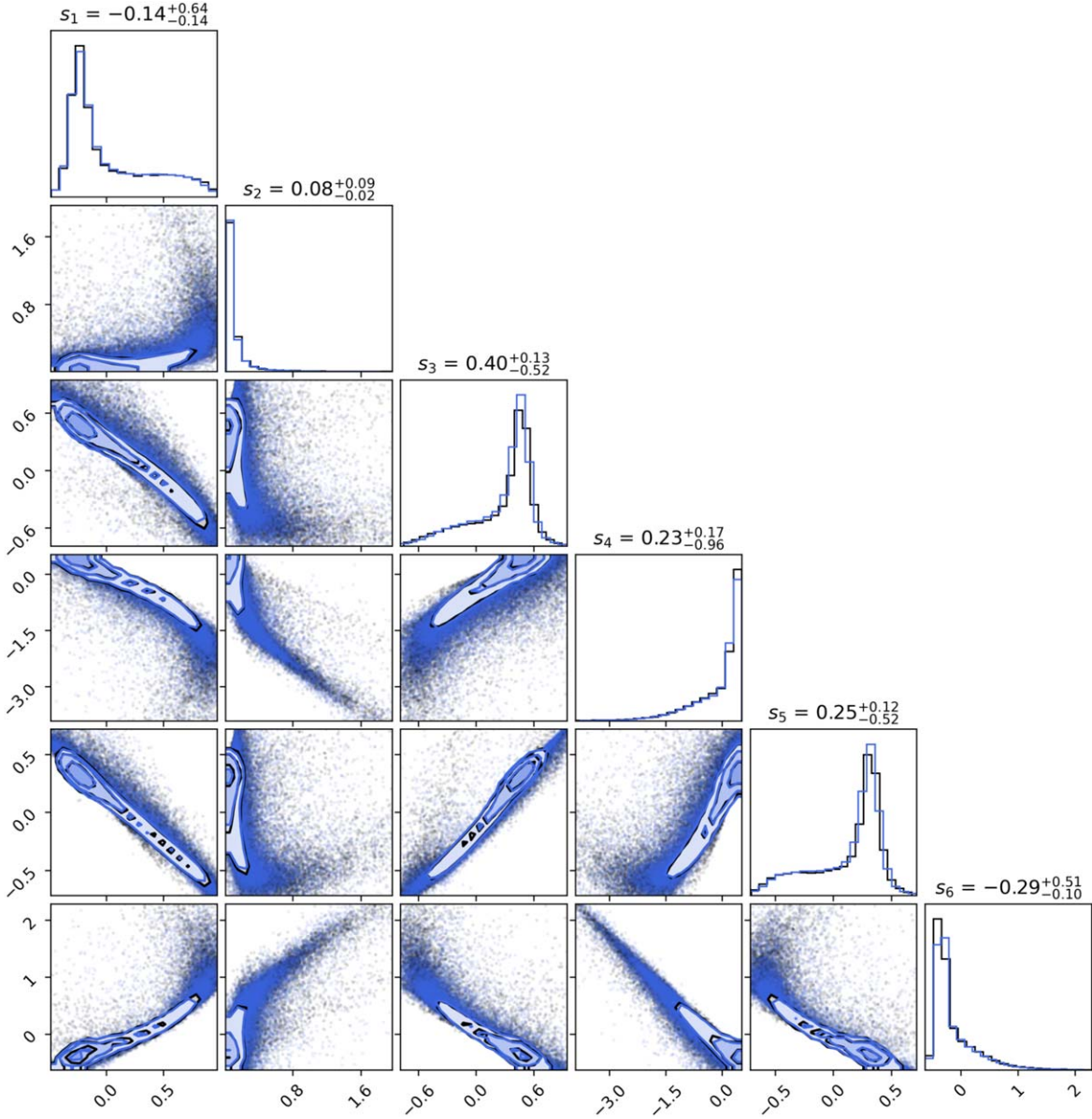


**Figure 5.** The latent space distribution of the validation data (black) and the distribution of the mock samples generated by the normalizing flow (blue) for each of the six latent variables.

or to spectra at  $z \approx 0$  (Traven et al. 2017). We see this capability as beneficial for subpopulations of galaxies where conventional spectrum analysis does not produce reliable parameter estimates, or none at all. Without the extended loss during training introduced in Section 3, the association between latent space position and physical parameters would be subject to random scatter from variations in redshift.

## 5. Outlier Detection

Because of our choice of additional loss terms, we surmise that the latent space is also well suited for outlier detection, as the anomalous samples will be pushed away from more typical ones. However, despite the apparent simplicity of the UMAP embedding in Figure 4, the latent space has a complex distribution in  $\mathbb{R}^S$ . Determining outliers in this space is not trivial. We therefore implement an additional mapping from the latent distribution of the SDSS galaxy sample to a  $S$ -dimensional normal distribution using a normalizing flow.

### 5.1. Normalizing Flow

A normalizing flow (NF; Papamakarios et al. 2017) consists of a series of trainable reversible transformations. Let us define  $f = f_i \circ f_2 \dots \circ f_n$  as the transformation from the base space  $\mathbf{u}$  to target space  $\mathbf{s}$ . Let  $\pi_s(\mathbf{s})$  be the target density and  $\pi_u(\mathbf{u})$  be some simple base density (i.e., Gaussian). The resulting model of the probability density in the target space is:

$$p(\mathbf{s}) = \pi_u(f^{-1}(\mathbf{s})) \left| \det \left( \frac{\partial f^{-1}}{\partial \mathbf{s}} \right) \right| \quad (6)$$

where  $\det(\partial f^{-1}/\partial \mathbf{s})$  is the Jacobian of the inverse transformation  $f^{-1}$ . It can be shown that maximizing the likelihood of data  $\log p(\mathbf{s})$  is equivalent to minimizing the Kullback–Leibler (KL) divergence between the proposed distribution and target distribution  $D_{\text{KL}}(\pi_s(\mathbf{s})||p(\mathbf{s}))$ .

To implement these transformations, we set up a five-layer masked auto-regressive flow (MAF) with 50 hidden features

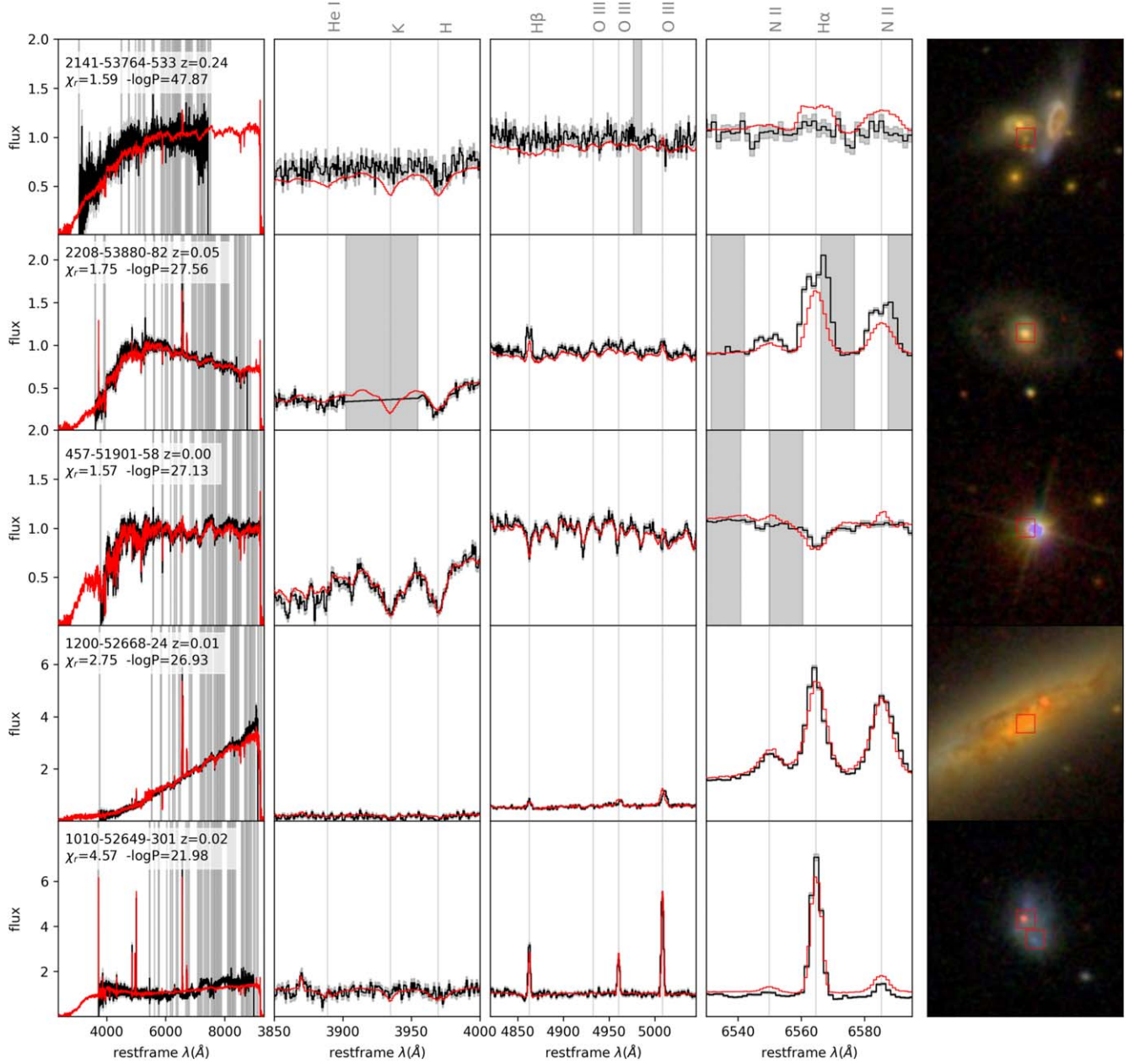


**Figure 6.** A sample of the outliers identified by the normalizing flow, ranked from top to bottom by the assigned probabilities, includes an interacting galaxy system, a double-peaked emission galaxy, a star misclassified as a galaxy, a galaxy with extreme dust attenuation, and a chance alignment of a WD-MS binary and background galaxy. The first column shows the entire normalized spectrum (black) with uncertainties (gray shading) and its reconstruction (red). The second, third, and fourth columns zoom in to important emission/absorption lines. The corresponding images are shown in the last column. The legend on the top left corner includes the SDSS ID, redshift, reduced chi-square, and the negative log probability of each spectrum.

using `nflows` (Durkan et al. 2020) and adopt the total negative log-likelihood as the loss function.

$$L_{\text{MAF}} = \sum_i \log p(s_i). \quad (7)$$

The entire SDSS galaxy samples are encoded by the best pretrained autoencoder, with 85% samples used for training and 15% for validation. We train the normalizing flow on an Intel CPU node with 4G RAM using 10,000 samples per batch and observe convergence after 2000 epochs.

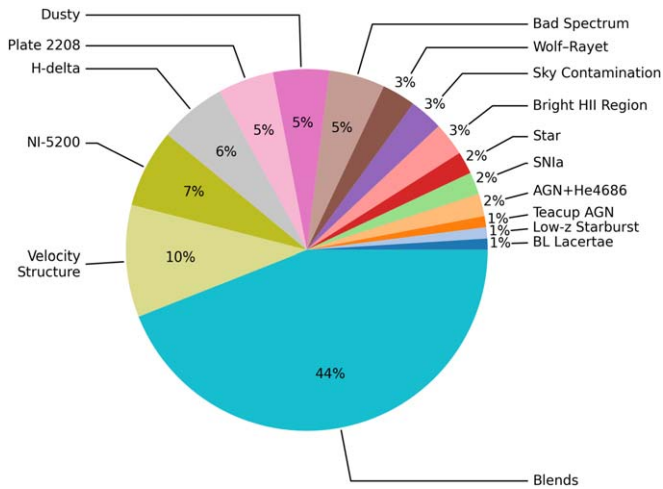
We test the performance of our normalizing flow by taking samples from the base distributions and using the model to transform them into the learned target distribution. As shown in

Figure 5, the distribution of the mock sample generated by the model and the true latent distribution of the validation set ( $N = 104,786$ ) are essentially indistinguishable.

### 5.2. Top-ranked Outliers

Having confirmed that the normalizing flow accurately reconstructs the encoded parameters of SDSS galaxies, we evaluate the likelihood for each spectrum in the base distribution, where the anomalous data will be assigned low likelihoods. We show a sample of the top-ranked, i.e., lowest probability, outliers in Figure 6.

For further analysis, we focus on the targets with low likelihood but good reconstruction quality, excluding the



**Figure 7.** Visual classification of 100 SDSS objects that are deemed most unlikely given their position in the SPENDER latent space.

strongest line emitters, for which the maximum flux is more than 100 times the continuum flux, as the SPENDER model often fails to accurately reproduce such strong emission lines. We visually inspect the SDSS spectra and images of the top 100 objects that are assigned the lowest likelihood, and find a variety of different objects, from blends to supernovae.

The largest group of NF outliers is formed by 44 blended objects—superpositions of multiple galaxies and/or stars. Identifying blends in images can be relatively straightforward, but detecting them from spectroscopic data is often challenging, especially when the spectra lack emission lines. Our method is particularly sensitive to blends, as the encoder could not easily reconcile the line and continuum features of the two objects with its expected spectrum shape of a single object. The NF anomaly detection is able to identify blends as outliers even when the spectra are almost featureless, which suggests that the autoencoder indeed has a reliable notion of the typical shape of a common continuum. In 31 of the 44 blends, the primary and secondary objects are well separated in the SDSS image. We present an example of such object, SDSS 2141-53764-533 ( $-\log p = 47.87$ ), a complex interacting system with long tidal tails, in the top row of Figure 6. In the remaining 13 blending systems, the primary and secondary objects are too close to be distinguished visually. In this case, we first subtract the best SPENDER model from data, then look for a second set of features in the residual spectrum. We show an example, SDSS 1010-52649-301 ( $-\log p = 21.98$ ), with interesting patterns in the residual spectrum in the last row of Figure 6. This system appears in a white dwarf-main-sequence binary catalog (Liu et al. 2012), and the strong emission lines suggest that is coincidentally aligned with a background galaxy.

We identified 10 emission-line galaxies with velocity structures, such as double-peaked emissions, and asymmetric lines. When an object with a velocity structure is resolved, we might observe some additional features in the image. For example, SDSS 2208-53880-82 ( $-\log p = 27.56$ ) has a ring-like structure that indicates rotational motion (Figure 6). Similarly, another example not shown here, SDSS 617-52072-326 ( $-\log p = 23.28$ ), also known as LEDA 2816158, is reported as interacting with a spiral companion (LEDA 2816157), confirmed by the long tidal tail in the image (Petrosian et al. 2002).

We found two stars that are misclassified as galaxies by the SDSS data pipeline, one of which is shown in the third row of Figure 6. K stars can mimic elliptical galaxies that lack emission lines. It is evident from the image that SDSS 457-51901-58 ( $-\log p = 27.13$ ) is a star because it has a morphology consistent with a single point-spread function, including visible diffraction spikes.

We found five extremely dusty objects with almost no blue-side emission. We show one example of a strongly reddened galaxy, SDSS 1200-52668-24 ( $-\log p = 26.93$ ), in the fourth row of Figure 6. Evidently, the  $H\beta$  emission is heavily suppressed compared to  $H\alpha$ , and the corresponding image clearly reveals the presence of dust clouds.

Two outliers, SDSS 2430-53815-267 ( $-\log p = 18.42$ ) and SDSS 1581-53149-470 ( $-\log p = 19.03$ ), are galaxies hosting supernovae that were active at the time when the spectra were taken. Both of them are reported as type Ia supernovae by Graur & Maoz (2013).

Some of the NF outlier spectra were already reported in the literature including: SDSS 277-51908-519 ( $-\log p = 18.45$ ) is identified as a BL Lacertae object by Peña-Herazo et al. 2021. SDSS 2745-54231-4 ( $-\log p = 18.17$ ) is selected by Lehmer et al. 2022 as a galaxy with unusually high specific star-formation rate ( $3.77^{+0.14}_{-0.10} \text{ yr}^{-1}$ ) and low metallicity ( $\sim 0.3Z_{\odot}$ ). SDSS 2145-54212-388 ( $-\log p = 19.86$ ) and SDSS 1998-53433-304 ( $-\log p = 21.18$ ) are star-forming galaxies showing strong nebular emission He II  $\lambda 4686$  that is believed to be dominated by emission from WolfRayet stars (Shirazi & Brinchmann 2012).

We classify five outlier spectra as “Bad Spectra” because a significant portion of them are missing, while the remaining parts are simply connected by straight lines.

Lastly, we found five outliers for which we could not find an explanation through visual inspection. However, we note that all of them stem from the same plate, 2208, taken on the same date, MJD 53880. One possible explanation is a subtle calibration mismatch for this plate.

The types of outliers we found are generally consistent with those identified by Baron & Poznanski (2017). We note that, in comparison, our method appears to be more sensitive to blends as outliers. A possible explanation could be our simultaneous use of line and continuum features, while their unsupervised random forest method considers each spectral bin separately.

We summarize our findings from the Top-100 outliers with our, admittedly subjective, classification in Figure 7. Note that there is no motivation for limiting the sample to 100 other than the time it takes to individually inspect and classify each spectrum. The labels we created for the above NF outliers describe only our best guess for its assigned low probability instead of a rigorous and quantitative analysis. We provide the full Top-100 outlier list in Table 2 and the NF probabilities for the entire SDSS galaxy sample at our code repository, and encourage interested readers to carry out their own follow-up studies.

## 6. Discussion and Conclusion

In this study, we performed unsupervised outlier detection on an interpretable, redshift-invariant encoding of SDSS galaxy spectra using the SPENDER architecture. Our best autoencoder model generates highly realistic spectra for the entirety of the SDSS spectroscopic galaxy sample with six latent parameters,



**Table 2**  
The Positions and Visual Classification Labels of the Top 100 SDSS Galaxy Outliers Ranked by Their Negative Log Probabilities  $-\log p$

Outlier 1–50					Outlier 50–100				
SDSS ID	R.A.	Decl.	$-\log p$	Label	SDSS ID	R.A.	Decl.	$-\log p$	Label
634-52164-68	310.92025	-6.20623	84.79	Blends	2268-53682-16	122.67157	13.11158	22.23	Blends
2753-54234-150	230.47445	12.39628	67.63	Blends	1789-54259-351	190.44328	10.21984	22.16	Bad Spectrum
346-51693-429	243.85497	0.65564	52.18	Blends	348-51696-444	248.53931	1.00628	22.06	Blends
1383-53116-293	221.50511	35.31970	51.83	Blends	1010-52649-301	159.86438	52.47833	21.98	Blends
1578-53496-55	241.85655	28.03230	51.75	Blends	1740-53050-182	140.44511	10.74848	21.95	Blends
2607-54184-354	203.65768	16.62918	51.57	Blends	653-52145-313	4.71200	-10.37686	21.75	Velocity Structure
2141-53764-533	222.01011	29.91320	47.87	Blends	1013-52707-127	170.24723	53.19049	21.49	Bright HII Region
2208-53880-85	246.49823	14.44520	46.48	Velocity Structure	1998-53433-304	159.05510	37.32432	21.18	WolfRayet
755-52235-410	115.89659	32.17637	44.88	Blends	2753-54234-408	230.15202	13.56871	21.16	Blends
2370-53764-120	148.09108	18.06227	42.26	Blends	541-51959-230	113.53775	31.97459	21.03	Sky Contamination
1574-53476-78	246.57670	24.55564	40.27	Blends	2885-54497-174	163.09376	8.98783	20.99	Bad Spectrum
1716-53827-156	225.08889	11.55063	39.82	Blends	2880-54509-269	185.47488	4.46184	20.98	NI-5200
489-51930-33	161.82787	65.11410	37.18	Blends	2245-54208-263	202.76555	25.84251	20.90	Strong H $\delta$
1980-53433-27	169.71192	38.24940	35.84	Blends	1876-54464-276	133.30146	63.49627	20.72	Blends
1708-53503-620	217.62451	13.65335	34.51	Teacup AGN	2208-53880-42	246.56421	14.24435	20.62	Plate 2208
1296-52962-221	124.98270	6.39953	31.92	Blends	2791-54556-390	223.44661	20.27430	20.60	Velocity Structure
348-51671-460	248.53931	1.00628	31.87	Star	2208-53880-127	245.99632	14.62167	20.41	Plate 2208
891-52584-89	120.29245	32.75213	29.97	Blends	1879-54478-496	148.67673	69.06061	20.21	NI-5200
2795-54563-133	234.11637	16.21026	29.62	Blends	627-52144-321	247.42806	47.29304	20.16	Bad Spectrum
2208-53880-265	245.79470	15.78185	29.47	Plate 2208	1442-53050-520	173.30839	47.04056	20.13	Bright HII Region
2170-53875-149	238.67295	17.30955	29.26	Blends	339-51692-306	195.06886	-2.90912	20.06	Strong H $\delta$
1713-53827-7	223.43381	9.09825	28.63	Sky Contamination	2208-53880-15	247.24661	14.57195	20.04	Blends
2598-54232-567	187.67913	18.76584	28.51	AGN+He4686	2145-54212-388	222.88978	26.76765	19.86	WolfRayet
1369-53089-530	181.55612	45.33371	28.49	Strong H $\delta$	1708-53503-256	216.14604	12.37499	19.81	Blends
2522-54570-408	239.28112	14.00622	28.26	Blends	1877-54464-240	138.94872	64.26537	19.75	Blends
1768-53442-243	187.46343	14.06649	28.09	Blends	776-52319-633	176.27600	62.31015	19.70	Strong H $\delta$
434-51885-137	116.84624	41.54075	27.69	Blends	1463-53063-523	202.48142	47.23385	19.60	NI-5200
2208-53880-82	246.45008	14.48492	27.56	Velocity Structure	593-52026-182	233.43788	2.71444	19.55	Blends
457-51901-58	44.43610	-8.51291	27.13	Star	1786-54450-372	136.14741	62.38961	19.53	Blends
2765-54535-484	226.65602	15.93717	26.98	Blends	486-51910-231	143.96497	61.35320	19.51	Dusty
1200-52668-24	138.81367	40.91724	26.93	Dusty	280-51612-172	170.54637	-0.07120	19.24	Sky Contamination
2570-54081-85	121.76227	7.49888	26.54	Blends	280-51612-213	170.24713	-0.38365	19.24	Blends
1798-53851-174	199.16677	9.57150	25.84	Bad Spectrum	307-51663-111	220.04478	-0.29398	19.23	NI-5200
892-52378-188	122.23627	35.27962	25.35	Blends	2207-53558-27	249.43996	16.59545	19.21	Velocity Structure
1359-53002-195	155.93396	41.06743	24.89	Blends	401-51788-423	25.06214	0.41179	19.13	Blends
1627-53473-611	188.57624	8.23982	24.34	WolfRayet	1581-53149-470	235.10316	32.86590	19.03	SNIIa
575-52319-200	155.91516	4.18628	24.34	NI-5200	638-52081-281	316.36185	-7.57458	19.02	Blends
931-52619-573	125.66402	31.50058	24.26	Blends	1677-53148-350	226.10314	44.41580	18.89	Velocity Structure
1608-53138-173	175.89681	11.95587	23.98	Bad Spectrum	2763-54507-360	220.84255	16.21258	18.79	Strong H $\delta$
1324-53088-240	210.72928	54.37413	23.90	NI-5200	1418-53142-370	239.62236	35.22463	18.67	AGN+He4686
1946-53432-30	148.30424	30.85623	23.84	Blends	551-51993-372	132.80788	50.67865	18.56	Dusty
617-52072-326	235.02012	57.25070	23.28	Velocity Structure	1740-53050-102	141.32669	10.50220	18.49	Velocity Structure
2208-53880-124	246.05605	14.66926	23.17	Plate 2208	277-51908-519	165.98395	0.37677	18.45	BL Lacertae
1999-53503-224	183.90322	33.52926	22.87	Blends	2430-53815-267	132.43307	12.29871	18.42	SNIIa
1767-53436-367	185.73890	15.86261	22.82	NI-5200	1269-52937-606	131.88764	31.02697	18.42	Velocity Structure
410-51877-620	44.88340	0.85483	22.57	Blends	2208-53880-281	245.33715	14.68445	18.36	Plate 2208
1721-53857-102	231.05243	8.54481	22.55	Dusty	1753-53383-252	170.07089	13.58969	18.31	Dusty
1740-53050-315	139.70837	10.57356	22.39	Blends	2477-54058-389	159.76004	23.51568	18.20	Strong H $\delta$
845-52381-246	187.91661	3.94210	22.29	Bright HII Region	2745-54231-4	214.19363	14.70976	18.17	Low-z Starburst
1835-54563-29	233.26141	4.20341	22.28	Velocity Structure	750-52235-326	358.94087	15.87922	18.00	Blends

which encode the physical properties probed by the galaxy spectra.

We defined a new loss term to directly relate distances in latent space to distances in rest-frame space, which discourages latent-space degeneracies that act as a source of stochasticity on any subsequent use of the latents. In particular, the decoder can learn a more robust and complete underlying rest-frame model over the entire redshift range. In addition, the association of latent-space position to physical properties is more stable and evident with such a robust encoding.

Training with similarity loss encourages physically similar galaxies to cluster in latent space, as long as there are enough intermediate objects to link them. This new loss term encouraged an encoding that is well suited for outlier detection: outliers are pushed away from more common samples, who themselves tended to cluster.

We trained a normalizing flow on the latent distribution of the entire SDSS galaxy sample and identified the top 100 objects that are deemed most unlikely by the normalizing flow model. By visual inspection and classification, we confirmed

that our anomaly detection method finds a wide variety of meaningful astrophysical and instrumental outliers. The most common group of outliers we found were due to the blending of multiple sources, either stars or galaxies. These blends were present in the SDSS main galaxy sample with high-quality redshifts. Were they to be used, e.g., in the training of photometric redshift estimators, they could cause erratic and suboptimal performance.

We caveat that outliers are, by definition, at locations in latent space that are sparsely populated. Because very little training data is available, both the encoding and the modeling by the normalizing flow are much less reliable for such objects. We therefore suggest considering the probability  $p(s)$  reported by the normalizing flow rather qualitatively: very low values indicate rare objects, but the exact values themselves may not be meaningful.






On the other hand, our immediate reason to utilize a normalizing flow, namely its fast evaluation of the sample likelihood, enables applications beyond outlier detection. In particular, it allows for rapid sampling from the latent distribution, which, coupled to the decoder, yields mock samples of realistic rest-frame spectra. As our architecture can adjust redshift, spectral resolution, and line-spread function, we can produce mock spectra for instruments or surveys other than SDSS. Furthermore, because of the clear association of physical parameters with latent-space position, one can estimate those parameters by encoding an unseen spectrum and then adopting the parameters of interest from neighbors in latent space, without the need for a full-fledged spectrum analysis pipeline. To support such applications, we make our new SPENDER model as well as the full catalog of latent-space probabilities available at our code repository.<sup>4</sup>

### Acknowledgments

The authors wish to thank Michael Strauss for his swift help with the visual inspection and classification of the outliers discussed in this paper. The authors would also like to thank Jiaxuan Li for his help in setting up the normalizing flow. This work was supported by the AI Accelerator program of the Schmidt Futures Foundation. The authors are pleased to acknowledge that the work reported on in this paper was substantially performed using the Princeton Research Computing resources at Princeton University which is a consortium of groups led by the Princeton Institute for Computational Science and Engineering (PICSciE) and Office of Information Technology's Research Computing.

*Software:* `Pytorch` (Paszke et al. 2019), `corner` (Foreman-Mackey 2016), `umap` (Sainburg et al. 2021), `accelerate` (Gugger et al. 2022), `torchinterp1d`, `nflows` (Durkan et al. 2020), `NumPy` (Harris et al. 2020), `Astropy` (Astropy Collaboration et al. 2022), `Matplotlib` (Hunter 2007).

### ORCID iDs

Yan Liang  <https://orcid.org/0000-0002-1001-1235>  
 Peter Melchior  <https://orcid.org/0000-0002-8873-5065>  
 Sicong Lu  <https://orcid.org/0000-0002-8814-1670>  
 Andy Goulding  <https://orcid.org/0000-0003-4700-663X>  
 Charlotte Ward  <https://orcid.org/0000-0002-4557-6682>

### References

- Ahumada, R., Prieto, C. A., Almeida, A., et al. 2020, *ApJS*, 249, 3  
 Astropy Collaboration, Price-Whelan, A. M., Lim, P. L., et al. 2022, *ApJ*, 935, 167  
 Baron, D., & Poznanski, D. 2017, *MNRAS*, 465, 4530  
 Bolton, A. S., Schlegel, D. J., Aubourg, É., et al. 2012, *AJ*, 144, 144  
 Brown, M. J., Moustakas, J., Smith, J.-D., et al. 2014, *ApJS*, 212, 18  
 Durkan, C., Bekasov, A., Murray, I., & Papamakarios, G. 2020, *nflows*: normalizing flows in PyTorch, v0.14, Zenodo, doi:10.5281/zenodo.4296287  
 Foreman-Mackey, D. 2016, *JOSS*, 1, 24  
 Graur, O., & Maoz, D. 2013, *MNRAS*, 430, 1746  
 Gugger, S., Lysandre Debut, T. W., Schmid, P., Mueller, Z., & Mangrulkar, S. 2022, Accelerate: Training and inference at scale made simple, efficient and adaptable, GitHub, <https://github.com/huggingface/accelerate>  
 Harris, C. R., Millman, K. J., van der Walt, S. J., et al. 2020, *Natur*, 585, 357  
 Hemmati, S., Capak, P., Pourrahmani, M., et al. 2019, *ApJL*, 881, L14  
 Hoyle, B., Rau, M. M., Paech, K., et al. 2015, *MNRAS*, 452, 4183  
 Hunter, J. D. 2007, *CSE*, 9, 90  
 Lehmer, B. D., Eufrazio, R. T., Basu-Zych, A., et al. 2022, *ApJ*, 930, 135  
 Liu, C., Li, L., Zhang, F., et al. 2012, *MNRAS*, 424, 1841  
 McInnes, L., Healy, J., & Melville, J. 2018, arXiv:1802.03426  
 Melchior, P., Liang, Y., Hahn, C., & Goulding, A. 2023, *AJ*, 166, 74  
 Pace, Z. J., Tremonti, C., Chen, Y., et al. 2019, *ApJ*, 883, 83  
 Papamakarios, G., Pavlakou, T., & Murray, I. 2017, Advances in Neural Information Processing Systems 30, ed. I. Guyon et al. (Red Hook, NY: Curran Associates, Inc.), [https://proceedings.neurips.cc/paper\\_files/paper/2017/file/6c1da886822c67822bcf3679d04369fa-Paper.pdf](https://proceedings.neurips.cc/paper_files/paper/2017/file/6c1da886822c67822bcf3679d04369fa-Paper.pdf)  
 Paszke, A., Gross, S., Massa, F., et al. 2019, in Advances in Neural Information Processing Systems 32, ed. H. Wallach et al. (Red Hook, NY: Curran Associates, Inc.), [https://proceedings.neurips.cc/paper\\_files/paper/2019/file/bdbca288fee7f92f2bfa9f7012727740-Paper.pdf](https://proceedings.neurips.cc/paper_files/paper/2019/file/bdbca288fee7f92f2bfa9f7012727740-Paper.pdf)  
 Peña-Herazo, H. A., Massaro, F., Gu, M., et al. 2021, *AJ*, 161, 196  
 Petrosian, A., McLean, B., Allen, R. J., et al. 2002, *AJ*, 123, 2280  
 Polletta, M., Tajer, M., Maraschi, L., et al. 2007, *ApJ*, 663, 81  
 Portillo, S. K., Parejko, J. K., Vergara, J. R., & Connolly, A. J. 2020, *AJ*, 160, 45  
 Ross, A. J., Bautista, J., Tojeiro, R., et al. 2020, *MNRAS*, 498, 2354  
 Sainburg, T., McInnes, L., & Gentner, T. Q. 2021, *Neural Computation*, 33, 2881  
 Salim, S., Boquien, M., & Lee, J. C. 2018, *ApJ*, 859, 11  
 Salim, S., Lee, J. C., Janowiecki, S., et al. 2016, *ApJS*, 227, 2  
 Serrà, J., Pascual, S., & Karatzoglou, A. 2018, in Artificial Intelligence Research and Development: Current Challenges, New Trends and Applications, ed. Z. Falomir, K. Gibert, & E. Plaza (Amsterdam: IOS Press), 120  
 Shirazi, M., & Brinchmann, J. 2012, *MNRAS*, 421, 1043  
 Sinha, S., & Dieng, A. B. 2021, in Advances in Neural Information Processing Systems 34, ed. M. Ranzato et al. (Red Hook, NY: Curran Associates, Inc.), [https://proceedings.neurips.cc/paper\\_files/paper/2021/file/6c19e0a6da12dc02239312f151072ddd-Paper.pdf](https://proceedings.neurips.cc/paper_files/paper/2021/file/6c19e0a6da12dc02239312f151072ddd-Paper.pdf)  
 Tojeiro, R., Heavens, A. F., Jimenez, R., & Panter, B. 2007, *MNRAS*, 381, 1252  
 Tojeiro, R., Percival, W. J., Heavens, A. F., & Jimenez, R. 2011, *MNRAS*, 413, 434  
 Traven, G., Matijević, G., Zwitter, T., et al. 2017, *ApJS*, 228, 24

<sup>4</sup> <https://github.com/pmelchior/spender>